

Unraveling Na-Ion Insertion Mechanisms in Polymer-Derived SiCN(O) Ceramic via Operando Raman Spectroscopy

Marco Melzi d'Eril,^{*[a]} Alexander Kempf,^{*[a]} Dario M. De Carolis,^[a]
Magdalena Joanna Graczyk-Zajac,^[a, b] Gabriela Mera,^[a] and Ralf Riedel^[a]

In this study we investigate the Na insertion process occurring in the “free carbon” phase embedded in two different SiCN(O) matrices with operando Raman spectroscopy. The two SiCN(O) samples have been prepared using two different thermal treatments carried out at 1000 °C (SiCN(O)1000) and 1400 °C (SiCN(O)1400). X-ray diffraction as well as argon adsorption reveal significant structural and morphological differences between the materials. SiCN(O)1000 shows an amorphous nature whereas SiCN(O)1400 reveals the presence of crystalline β-SiC, accompanied by a notable increase in surface area (from 56.7 m²/g to 331 m²/g) and micropore volume (from 0.02 cm³/g to 0.12 cm³/g). These alterations in the ceramic matrix due to thermal treatment affect significantly the electrochemical performance with initial de-sodiation capacities of 112.4 mAh/g

and 52.3 mAh/g for SiCN(O)1000 and SiCN(O)1400, respectively. Operando Raman spectroscopy, carried out during the sodiation and de-sodiation of the SiCN(O) ceramics, reveals the microstructural changes occurring to the “free carbon” phase during the storage of sodium ions. As sodium is inserted, a shift in the G-band position is observed in both the samples from about 1600 cm⁻¹ to 1555 cm⁻¹, with a concomitant decrease of the D-band intensity and the distance between defects (L_D) growing from 7.5 nm to 17.5 nm. Upon de-sodiation, SiCN(O)1400 exhibits an inferior storage reversibility compared to SiCN(O)1000. This may be attributed to the irreversible sodium trapping occurring in SiCN(O)1400, highlighted by the reduced efficiency of the electrochemical process.

Introduction

With the incessant electrification of modern society, batteries have become a cornerstone of our standard of living. Lithium-ion batteries (LIBs) have long been the dominant technology, offering remarkable stability and energy density. However, the scarcity of lithium resources and the volatile nature of its market price, influenced by geopolitical factors, have fueled the quest for alternative battery technologies that rely on abundant and cost-effective materials.^[1,2] Sodium serves as an attractive alternative due to its virtually limitless resources and comparatively lower price.^[3,4] In recent years, polymer-derived ceramics (PDCs) with high carbon content have gained attention as

promising materials for energy storage applications thanks to their light weight, high electrical conductivity and chemical resistance.^[5] Numerous studies have addressed their functionality and demonstrated their suitability for both lithium-based^[6–12] and sodium-based batteries.^[13–17] Among them, silicon oxycarbonitride (SiCN(O)) has attracted attention due to its ability to serve as a porous matrix for reversible plating of metallic sodium on its surface.^[18] This class of ceramic materials possess a complex structure comprising a ceramic matrix containing embedded “free carbon” phase. While it is acknowledged that the presence of embedded “free carbon” certainly contributes to the insertion storage mechanism and its amount influences the final capacity,^[19,20] further research is necessary to gain a more comprehensive understanding of these phenomena.^[13] To unravel the intricate mechanisms governing the energy storage capabilities of SiCN(O), advanced characterization techniques are essential. In this regard, in-situ Raman spectroscopy represents a powerful tool,^[21–24] allowing for real-time monitoring and understanding of the Na-ion storage mechanism. We place a significant emphasis on the detailed examination of Raman band shifts and intensity alterations, associating them with an interpretation of the electrochemical processes unfolding within the matrix. In this investigation, we employ a combination of electrochemical characterization, structural analysis, and operando Raman spectroscopy to gain deeper insights into the influence of both amorphous mixed-bonded state ($\text{SiC}_x\text{N}_y\text{O}_z + \text{C}_{\text{free}}$)^[25] and crystalline structures (β-SiC) within the SiCN(O) matrix, with particular regard to the role of “free carbon” in the insertion mechanism. For this purpose,

[a] M. Melzi d'Eril, A. Kempf, D. M. De Carolis, M. J. Graczyk-Zajac, G. Mera, R. Riedel
Department of Material Sciences,
Technical University of Darmstadt
64287 Darmstadt, Germany
E-mail: marco.melzi@tu-darmstadt.de
alexander_martin.kempf@tu-darmstadt.de

[b] M. J. Graczyk-Zajac
EnBW Energie Baden-Württemberg AG
Durlacher Allee 93
76131 Karlsruhe, Germany

 Supporting information for this article is available on the WWW under
<https://doi.org/10.1002/batt.202400029>

 © 2024 The Authors. Batteries & Supercaps published by Wiley-VCH GmbH.
This is an open access article under the terms of the Creative Commons Attribution License, which permits use, distribution and reproduction in any medium, provided the original work is properly cited.

two distinct samples have been prepared and thermally treated at 1000 °C and 1400 °C respectively. The resulting ceramics exhibit different porosity and morphological structure which affect the storage mechanism and reversibility of the process. The “free carbon” phase contained in the ceramics has been compared with fructose-derived hard carbon (HC) highlighting structural similarities. This points out a similar storage mechanism as in HC which is confirmed by the operando Raman results.

Experimental

SiCN(O) Synthesis

The pre-ceramic material has been produced by cross-linking perhydropolysilazane (PHPS) with divinylbenzene using a Pt-catalyst ($\text{Pt}^{(0)}$ -1,3-divinyl-1,1,3,3-tetramethyldisiloxane, diluted in xylene, Sigma-Aldrich, UK) at 120 °C for 6 h. The cross-linked pre-ceramic compound is then pyrolyzed in a quartz tube furnace under Ar atmosphere at 1000 °C using a heating rate of 150 °C/h and a holding time at the maximum temperature of 2 h.^[26] This resulting ceramic sample will be addressed as SiCN(O)1000. Starting from the pyrolyzed material, a further annealing step at a higher temperature has been carried out. Some SiCN(O)1000 is placed in a tubular alumina furnace under Ar atmosphere and brought to 1400 °C using the same heating rate and holding time as for the SiCN(O)1000. The obtained material is referred to as SiCN(O)1400. Both samples are ground in a mortar and subsequently in a ball mill (Rocker Mill MM 400, Retsch, Germany) and eventually sieved down to <40 µm. Additionally, for comparison purposes, a HC sample has been produced by pyrolysis of fructose (Sigma Aldrich, England) at 1100 °C under Ar atmosphere with a heating rate of 100 °C/h and a holding time at 1100 °C of 6 h.

Electrode Preparation

Electrodes have been prepared by mixing the ceramic powder with water-based binders and carbon black in the weight proportions listed in (Table 1).

The components of the slurry have been dispersed using an Ultra Turrax (IKA-Werke, GmbH) and water has been added to obtain the desired viscosity. The slurry has been printed on an Al foil using a doctor blade and subsequently, the water has been removed by placing the printed foil in a dryer at 40 °C. The electrodes have been stamped out in a round shape using a cutter and vacuum-dried with a vacuum oven (B-580 Glass Oven) at 80 °C for 24 h.

Characterization Methods

Argon Gas Adsorption

Gas adsorption isotherms have been acquired at 87 K using a 3P-micro300 (3P Instruments, Germany) and Ar as adsorbate. The samples have been dried under vacuum for 16 h at 100 °C before the measurement. The pore size distribution has been calculated according to the BJH method whereas the specific surface area (SSA) has been determined using the BET theory.

X-Ray Diffraction

A STOE STAD1 P diffractometer (STOE & Cia GmbH, Germany) equipped with monochromatic Mo-K α radiation ($\lambda=0.07093\text{ nm}$) has been used to measure the X-rays diffractograms of both ceramics in the range between 5° and 45°.

Chemical Composition

The chemical composition of both ceramics has been carried out by the Mikroanalytisches Labor Pascher via ICP. Carbon analysis has been performed using conductometric detection after combustion or melting. Silicon analysis has been conducted via Inductively Coupled Plasma – Atomic Emission Spectroscopy (ICP-AES) following fusion digestion whereas nitrogen analysis has been carried out using a thermal conductivity measurement cell after Carrier Gas Hot Extraction (CGHE) and lastly oxygen analysis has been accomplished through IR (Infrared) detection subsequent to CGHE. To calculate the amount of the free carbon phase in the resulting SiCN(O) ceramic, it is assumed that oxygen is bonded to silicon as SiO_2 , nitrogen and silicon form Si_3N_4 and the remaining Si is bonded to C in the form of SiC. The excess carbon is assumed to exist as free carbon.^[27,28]

Electrochemical Cycling

The long term galvanostatic cycling with potential limitation (GCPL) measurements have been carried out on a Biologic VMP3 within a potential range of 2.5 V to 0.005 V and a current density of 37.2 mAh/g for 100 cycles. For the operando Raman investigation, the cells have been cycled using a portable Biologic SP-150 (Biologic, France) choosing a constant current value which limited the charge/discharge rate to C/3 and the potential range between 2.5 V and 0.005 V. All the voltages in this work have to be intended as vs. Na/Na⁺.

Raman Spectroscopy Investigation

The Raman measurements have been performed using a LabRAM Horiba HR spectrometer HR800 equipped with a 514.5 nm laser (Cobolt Fandango™ 100). Raman spectra of both pristine ceramics have been compared with HC (spectra visible in the SI). Numerical calculation of the crystallite size L_a enables the quantification of the

Table 1. Compositional ratio of the slurry used to print the electrodes.

Material	Wt.%	Composition	Function
SiCN(O)1000/1400	94	Powder	Active Material
Carbon Black	2	Powder (TIMCAL Super P Conductive)	Enhance Conductivity
Carboxymethylcellulose (CMC)	2	5 wt.% in H ₂ O (Sigma-Aldrich)	Binder
Styrene Butadiene Rubber (SBR)	2	40 wt.% in H ₂ O/Ethanol (Vol. 3:7) (Zeon)	Binder

structural order, facilitating a comparison of the amorphous structure of carbon. The calculation of L_a has been based on equation (1),^[29] utilizing the integrated intensities obtained after the deconvolution of the Raman bands. Band shapes and Raman shifts are listed in Table 2, the deconvoluted spectra can be found in Figure S1, S2, S3 in the supporting information (SI).

$$L_a = (2.4 \times 10^{-10}) \lambda_i^4 \left(\frac{I(A_D)}{I(A_G)} \right)^{-1} \quad (1)$$

An ECC-Opto-10 cell (EL-CELL GmbH, Germany) with the electrodes in a side-by-side geometry has been used for the in-situ measurements. As visible in Figure 1, a sapphire glass window allows one side of the cell to be exposed to the laser. The electrode made out of the ceramic material has been subjected to cycling against metallic sodium in a half-cell configuration, utilizing a sodium disc as a reference. For the experiments, both electrodes were cut into

stripe shapes, approximately 2 mm×7 mm in size, using scissors. Before sealing the cell with the top cover, a few drops of the 1 M NaPF₆ EC:DEC (3:7)+5 wt.% FEC electrolyte were applied to the separator. Preliminary tests were conducted to observe the influence of the solid electrolyte interface (SEI) formation during the first cycle on the Raman spectra. Afterwards, each material underwent more than 20 cycles and simultaneously Raman spectra have been acquired every 25 mV (when possible) during selected cycles. The focus has been placed on the changes in reversibility throughout cycling, hence the measurements took place during the second cycle and were repeated after more than 20 cycles. The first cycle has been excluded from the analysis due to the influence from SEI formation. To enable acquisition within the smallest voltage range possible, all Raman measurements were conducted under rapid acquisition settings. Frequent re-focusing of the instrument has been necessary during the measurements due to the evolving nature of the system. Given the geometry of the cell, the measuring spot has been set close to the anode's edge facing the Na counter electrode being this area the first subjected to the sodiation. The upper face of the anode is in direct contact with the sapphire glass window leaving barely space for the electrolyte and therefore limiting the ion transport to the center of the electrode. As a result, sodiation of the material initiates at the electrode's border, with ions subsequently diffusing throughout the material. The measurement spot has been regularly slightly shifted after a few acquisitions to prevent localized burning of the electrode and decomposition of the electrolyte. The aforementioned factors complicate the process of obtaining high quality Raman spectra. Therefore, the focus has been placed on the first order Raman bands of carbon, for which meaningful intensities could be recorded. SiCN electrodes consist of 2 wt.% of carbon black ensuring the electronic conductivity of the composite electrode. Carbon black is also Raman active^[30] and might lead to perturbing signals during investigation of Li-ion cells by Raman

Table 2. Parameters used for the deconvolution of the Raman spectra of the pristine powder materials.

Deconvolution peak	Band shape	Raman shift (cm ⁻¹)
T	Lorentz	1140–1173
D	Lorentz	1336–1349
D''	Gaussian	1539–1553
G	Lorentz	1589–1597
T+D	Lorentz	2436–2504
2D	Lorentz	2646–2682
D+G	Lorentz	2908–2916
2G	Lorentz	3125–3250

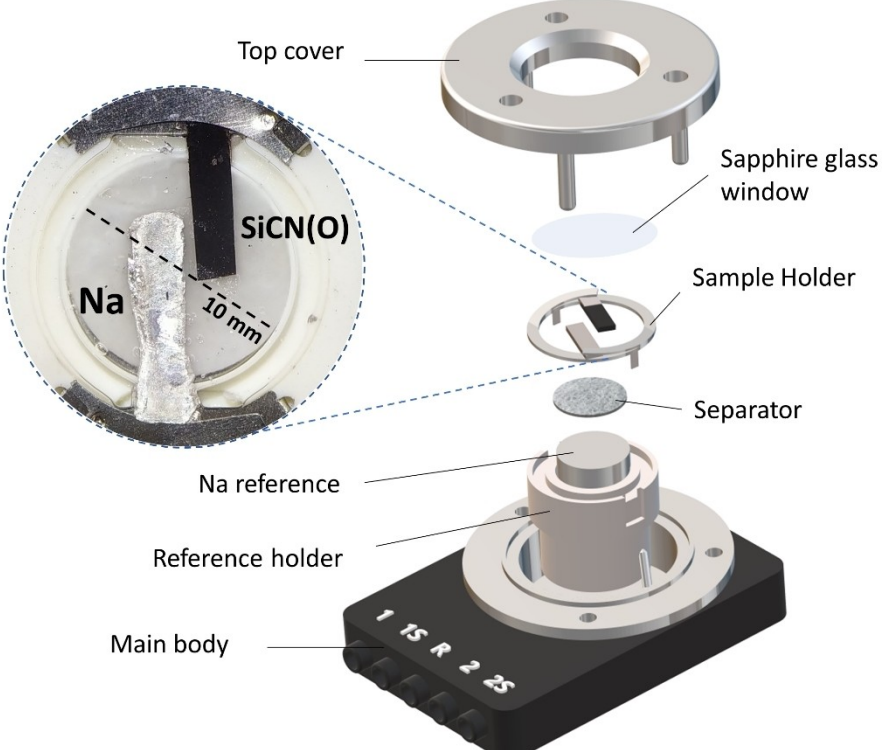


Figure 1. Schematic representation of the side-by-side geometry of the cell used for this work.

spectroscopy.^[31] Nevertheless, according to the recent report on Raman spectroscopy investigation of negative electrode materials for sodium-ion batteries, it is commonly accepted to neglect its influence, even if representing 5 wt.% of the electrode composition.^[32] Moreover, carbon black is essential to ensure the electrochemical performance of the cell. Our experiments aim for Raman analysis under the “usual” cycling conditions, thus with conductive additives. Similar attempts have been already reported in the literature.^[24] Additional contribution of the electrolyte needs to be considered for the deconvolution of the spectra, with mainly two bands appearing within the investigated range. A spectrum of the electrolyte can be found in the SI (Figure S4). The fitting parameters used for the analysis of the operando Raman spectra are summarized in Table 3.

The distance between defects, L_D , has been calculated using equation (2).^[33]

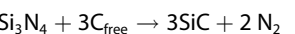
$$L_D^2 = 1.8 \times 10^{-9} \lambda_L^4 \left(\frac{I_D}{I_G} \right)^{-1} \quad (2)$$

Results and Discussion

The XRD pattern of sample SiCN(O)1000 reveals the amorphous nature of the material. After annealing at 1400 °C the appearance of the three reflections respectively at 16.19°, 26.61° and

Table 3. Fitting parameters used for the deconvolution of the operando Raman spectra.		
Deconvolution peak	Band shape	Raman shift (cm^{-1})
Electrolyte	Gaussian	1115–1125
T	Lorentz	1100–1250
D	Lorentz	1315–1375
Electrolyte	Gaussian	1455–1461
D'	Gaussian	1485–1530
G	Lorentz	1540–1620

31.31° proves the presence of β -SiC (Figure 2a) resulting from the carbothermal reduction according to the chemical formula:



This process results in a loss of material (N_2 gas), which significantly alters the microstructure of the ceramic, leading to a considerable increase in internal surface area and porosity. This observation is supported by gas adsorption measurements (see the Ar-adsorption/desorption isotherms in Figure 2b). By applying the BET theory to both samples, a specific surface area (SSA) has been calculated, revealing a six-fold higher internal surface area for SiCN(O)1400. The average diameter and volume of the macropores are comparable in both samples (Figure 2c). However, there is a significant difference in the size of the mesopores, as indicated in Table 4. Furthermore, the sample SiCN(O)1400 exhibits a higher mesoporous volume, indicating an enhanced presence of smaller mesopores. Both samples have a comparable micropores average diameter, but sample SiCN(O)1400 has approximately six times greater micropore volume, demonstrating the significant influence of the thermal treatment on the ceramic's microstructure.

Both samples have been tested to compare their electrochemical sodium storage performance over 100 cycles applying a current equal to 37.2 mA/g. During the first cycle, sample SiCN(O)1000 exhibits a de-sodiation capacity of around 113.4 mAh/g which is more than double compared to that of SiCN(O)1400 equal to 52.1 mAh/g as shown in Figure 3.

Table 5 shows the results of the elemental analysis of the investigated materials. The amount of “free carbon” is comparable for both samples and, by itself, cannot account for the capacity difference registered along 100 cycles. Conversely, the elemental analysis revealed a significant drop in the amount of nitrogen and oxygen for SiCN(O)1400 accompanying the formation of crystalline β -SiC on the expense of amorphous

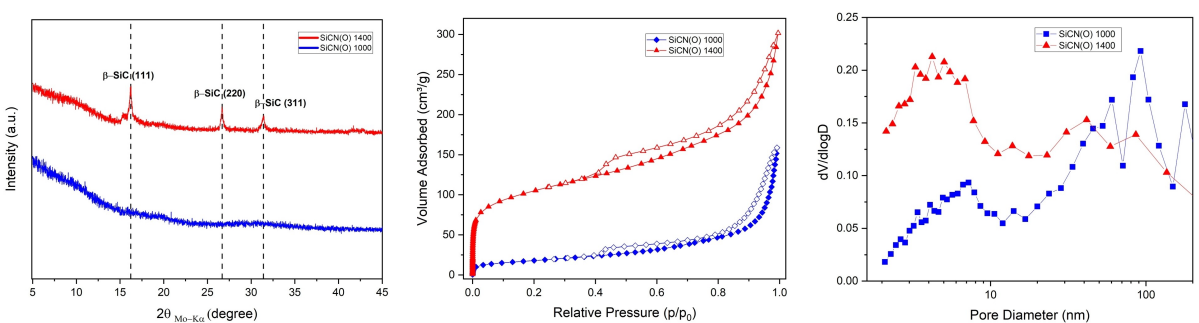


Figure 2. a) X-ray diffractogram b) adsorption isotherms and c) pore size distribution of the SiCN(O)1000 and SiCN(O)1400 ceramic samples.

Table 4. Porosity and density data of the SiCN(O)1000 and SiCN(O)1400 ceramics.

Sample	Porosity (%)	SSA (m^2/g)	Mesopores		Micropores	
			Avg. Pore Diameter (nm)	Pore Volume (cm^3/g)	Avg. Pore Diameter (nm)	Pore Volume (cm^3/g)
SiCN(O)1000	52.4	56.7	43	0.21	0.98	0.02
SiCN(O)1400	55.7	331	14	0.31	0.87	0.12

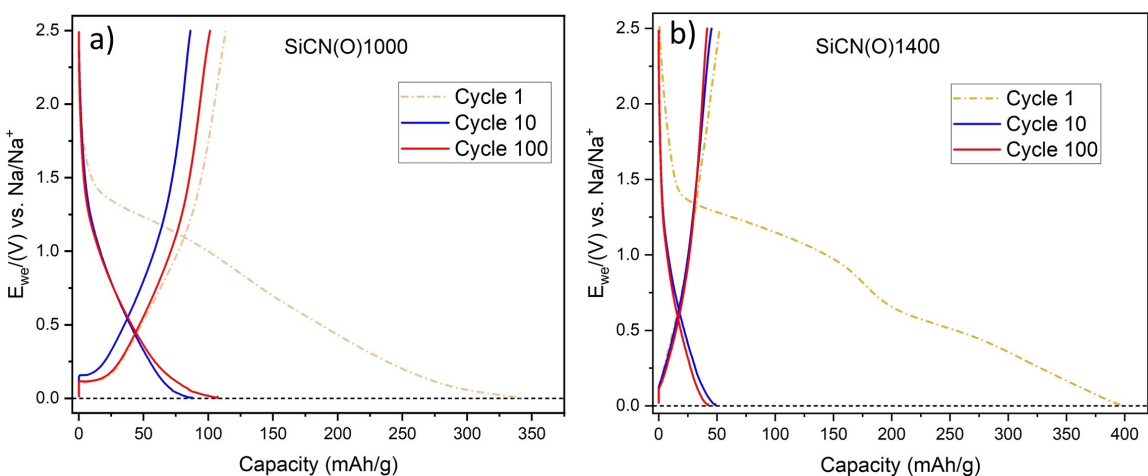


Figure 3. Voltage profiles showing the electrochemical performance of a) SiCN(O)1000 and b) SiCN(O)1400.

Table 5. Elemental contents, composition, stoichiometry and carbon crystallite size of the samples SiCN(O)1000 and SiCN(O)1400. L_a and first de-sodiation capacity of HC have been measured for comparison.

	SiCN(O)1000	SiCN(O)1400	Hard Carbon
L_a (nm)	5.1	6.8	6.3
Total Si wt.%	27.07 ± 0.37	30.33 ± 0.29	-
Total N wt.%	9.91 ± 0.19	3.46 ± 0.02	-
Total O wt.%	8.16 ± 0.04	2.06 ± 0.01	-
Total C wt.%	51.93 ± 0.08	61.71 ± 0.44	-
C-free wt.%	49.8	51.7	-
Stoichiometry	$Si_{1.00}C_{0.19}N_{0.73}(O_{0.53}) + C_{free4.30}$	$Si_{1.00}C_{0.77}N_{0.24}(O_{0.12}) + C_{free3.99}$	-
De-sodiation capacity @ cycle 1 (mAh/g)	112.4	52.3	70.5

mixed-bond structures. Considering that the amount of “free carbon” in SiCN(O)1000 and SiCN(O)1400 is nearly identical, the origin of the capacity difference can be attributed to additional storage sites in the mixed-bonded structure of SiCN(O)1000. On the other hand β -SiC is known to be electrochemically inactive without going through a surface modification process.^[34–36] Similar observations have been made for the intercalation of lithium into SiOC and SiCN ceramics.^[12,37] Raman spectroscopy and the deconvolution of the obtained spectra (in Figure S1, S2 and S3 in the SI) allowed to calculate the crystallite size (L_a) in order to compare the structural characteristics of the segregated “free carbon” in the ceramic matrix with a deeply investigated type of carbonaceous material such as HC.^[38]

The L_a size and Raman spectra demonstrate that the “free carbon” and the HC (derived from fructose) share structural similarities raising the expectation that the “free carbon” embedded in the ceramic matrix accommodates the Na-ions with a comparable mechanism as for HCs.^[32,39] Operando Raman has been measured to confirm this hypothesis with the prospect to see changes in the carbon spectra during sodiation and de-sodiation. Preliminary measures show that during the first cycle the SEI forming on the anode’s surface induces fluorescence which can overlay the Raman spectrum making the focusing non-trivial. To prevent the concealment of these

information and avoid to focus on an evolving system, the spectra have been collected during the second cycle where the SEI already formed and the system is more stable. For the SiCN(O)1000 sample the effects of the fluorescence become visible at around 1.5 V when the SEI begins to form (see Figure 4). This effect has already been reported for HC.^[32] However, fluorescence is observed even in the following cycles resulting from the presence of Na inserted into the graphitic structure. This phenomenon is reversible and the fluorescence disappears once the material has been de-sodiated (Figure S5 in the SI). The insertion of dopant elements in graphitic structures is known to affect the electronic properties of the material therefore inducing in some cases fluorescence.^[40] This effect makes the evaluation of the D- and G- band position and their intensities challenging.

The sodiation of the electrode resulted for both samples in the shifting of the G-band position (Figure S6 in the SI combines the voltage profile with the G-band position) and strong diminishing of the D-band intensity (see Figure 5). The source of the D-band has been a long-time matter of debate. Early theories claimed that the presence of defects would reduce the symmetry, therefore, activating Raman-inactive modes.^[41] Nevertheless, this theory was not able to explain the D-band shift when using different laser wavelengths. The

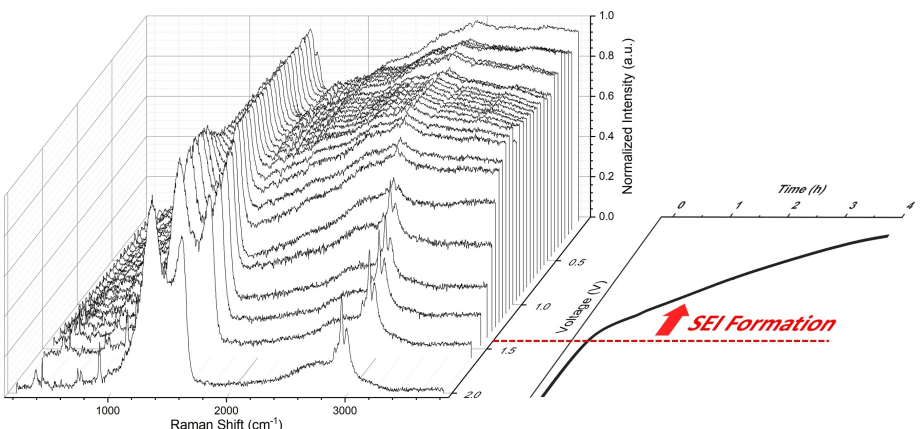


Figure 4. A 3D plot illustrating the acquired spectra during the first cycle of SiCN(O)1000. The SEI formation (marked with a red line) begins close to 1.5 V resulting in the fluorescence of the sample. The Voltage/Time profile depicting the first sodiation process is presented on the right-hand side.

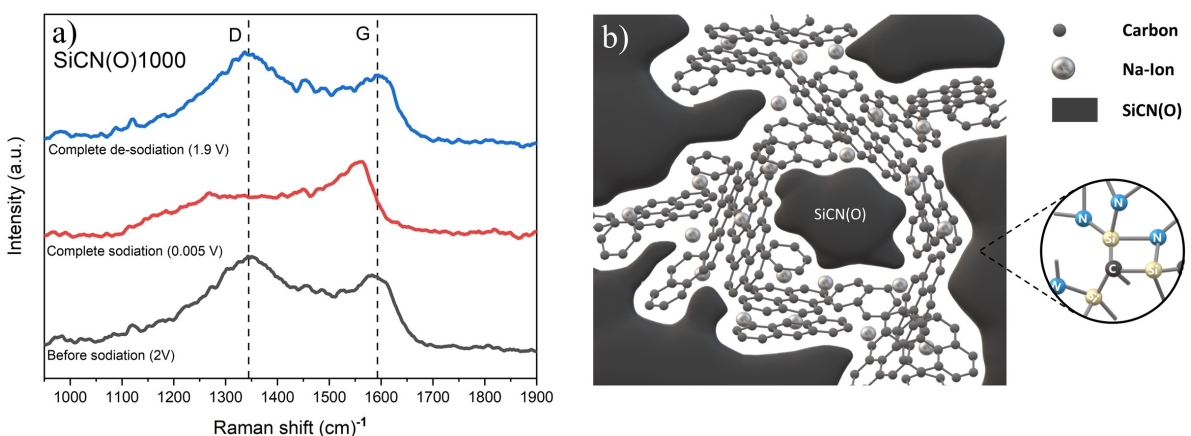


Figure 5. a) D- and G-band shifting during sodiation and de-sodiation of SiCN(O)1000 in the 2nd cycle. The disappearance of the D-band is visible in the fully sodiated status. b) Graphical representation of the SiCN(O) structure.

double resonance Raman theory (DRR) allows to explain this phenomenon.^[42] A short explanation of the first-order Raman scattering helps to introduce the D-band source. In this first scenario, only zone-center (Γ point) phonons are considered. When a photon ($\hbar\omega$) interacts with the considered material an electron-hole pair is created. The electron is excited to a virtual state and inelastically interacts with the crystal lattice emitting a phonon with zero momentum ($\hbar\omega_{\text{Phonon}}, q=0$). This condition prevents the electron from reaching other points in the reciprocal lattice.^[43] Once the electron-hole pair recombines, a photon with reduced energy ($\hbar\omega - \hbar\omega_{\text{Phonon}}$) is emitted. This energy loss is therefore the fingerprint of the material and in carbonaceous structures is associated to the G-band. In a second-order Raman scattering the phonon momentum is not zero and can scatter the electron from one point of the Brillouin zone to another. Under these conditions, the electron could scatter again either a second time with the lattice or elastically with a defect. For the sake of simplicity, we consider only the phonon-defect scattering for this theoretical background. Further details can be found elsewhere.^[43,44] Once the electron-hole pair recombines, a photon is emitted in the same way as for the first-order scattering with the difference that the

different phonon modes with $q \neq 0$ contribute to the Raman spectrum generating secondary bands (D-band, 2D-band etc.).^[45] For the DRR process to take place, two main conditions must be fulfilled: firstly, the analyzed sample must contain defects and secondly, the generation of electron-hole pairs has to be possible. This is the case if a band crossing in the vicinity of the fermi level is allowed. During sodiation of HC, the generation of an electron-hole pair is progressively hindered by the increasing presence of Na inserted in the structure.^[39] According to Reddy et al. during the sodiation process of HCs sodium inserts at defective sites.^[32,39] This hinders the fulfillment of the second requirement in the DRR theory, ultimately resulting in the gradual fading of the D-band. As the material undergoes complete sodiation, it is clear that the D-band intensity diminishes. This is exemplified by the behavior of sample SiCN(O)1000, as illustrated in Figure 5 a). SiCN(O)1400 shows, similarly as for SiCN(O)1000, the band shifting and D-band attenuation (see Figure S7).

The calculation of the distance between the defects (L_D) using equation (2) substantiates this explanation as visible in Figure 6. The inter-defect distance increasing along the sodiation points out that several sites are occupied by Na-ions during

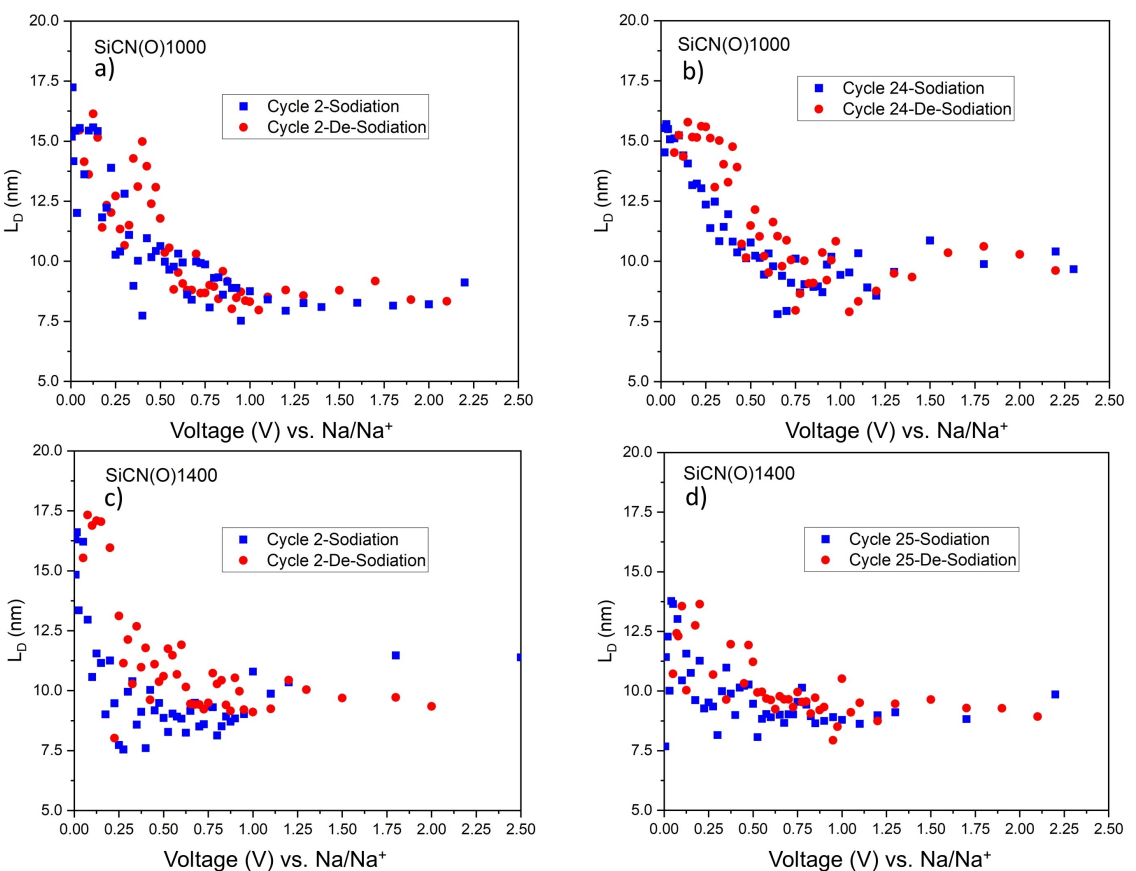


Figure 6. Shows the inter-defect distance values increasing during sodiation when defects are occupied by Na-ions and reversibly decreasing during de-sodiation comparing both materials in the second cycle a,c) and in a later cycle b,d).

the process. Nonetheless, the process is reversible, and during de-sodiation, the parameter's initial value is recovered.

However, in all measurements the D-band does not completely vanish and remains partially visible even at the fully sodiated state. This finding may in part be attributed to the geometry of the cell. Due to the small dimensions of the electrode and the relatively fast cycling rate, it is possible that some areas in the electrode were not fully sodiated but were included in the laser acquisition spot, thereby contributing to the weak presence of the D-band. Additionally, a secondary contribution to the D-band signal may arise from embedded carbon that does not participate in the insertion process and still satisfies the conditions for the DRR. Notably, the G-band position shifts during the sodiation of the ceramic. Previous studies have already reported the strong sensitivity of the G-band energy to the presence of dopant elements in graphitic structures.^[46,47] A similar trend is found for the amorphous "free carbon" embedded in the ceramic matrix. However, it is worth noting that the original positions of the bands can be recovered once the de-sodiation process is complete. To better visualize this behavior, the positions of the fitted G-band for both samples have been plotted against the cell potential (see Figure 7).

Both SiCN(O)1000 and SiCN(O)1400 exhibit a stable G-band position (around 1600 cm^{-1} and 1590 cm^{-1} , respectively) from

the open circuit voltage down to around 1 V (Figure 7a,c). However, beyond this voltage, the G-band position undergoes a continuous shift, reaching 1555 cm^{-1} at the fully-sodiated state (0.005 V) for both materials. SiCN(O)1000 demonstrates a high degree of overlap between the G-band positions during sodiation and de-sodiation both in the 2nd cycle as well as in the 24th. This suggests a notable level of reversibility in the structural changes induced by sodium. In contrast, SiCN(O)1400 displays a substantial hysteresis between the sodiation and de-sodiation curves, which is attributed to its high porosity. The sixfold larger internal surface area of SiCN(O)1400 compared to that of SiCN(O)1000 together with the higher porosity and smaller size of the pores provide more sites for the irreversible trapping of sodium ions. However, this behavior tends to diminish in the 25th cycle (see Figure 7d), corroborating the thesis of the irreversibly trapped Na ions. During the initial cycles, several structures and sites become permanently filled with sodium until they are no longer available, while the remaining active sites in the "free carbon" exhibit a high level of reversibility. SiCN(O)1400 experiences a shift in the initial position of the G-band to a higher value (1600 cm^{-1}) after more than 20 cycles (Figure 7d), indicating a definitive change within the carbon structure, which may result from irreversible accommodation of sodium within the pores. This trapping

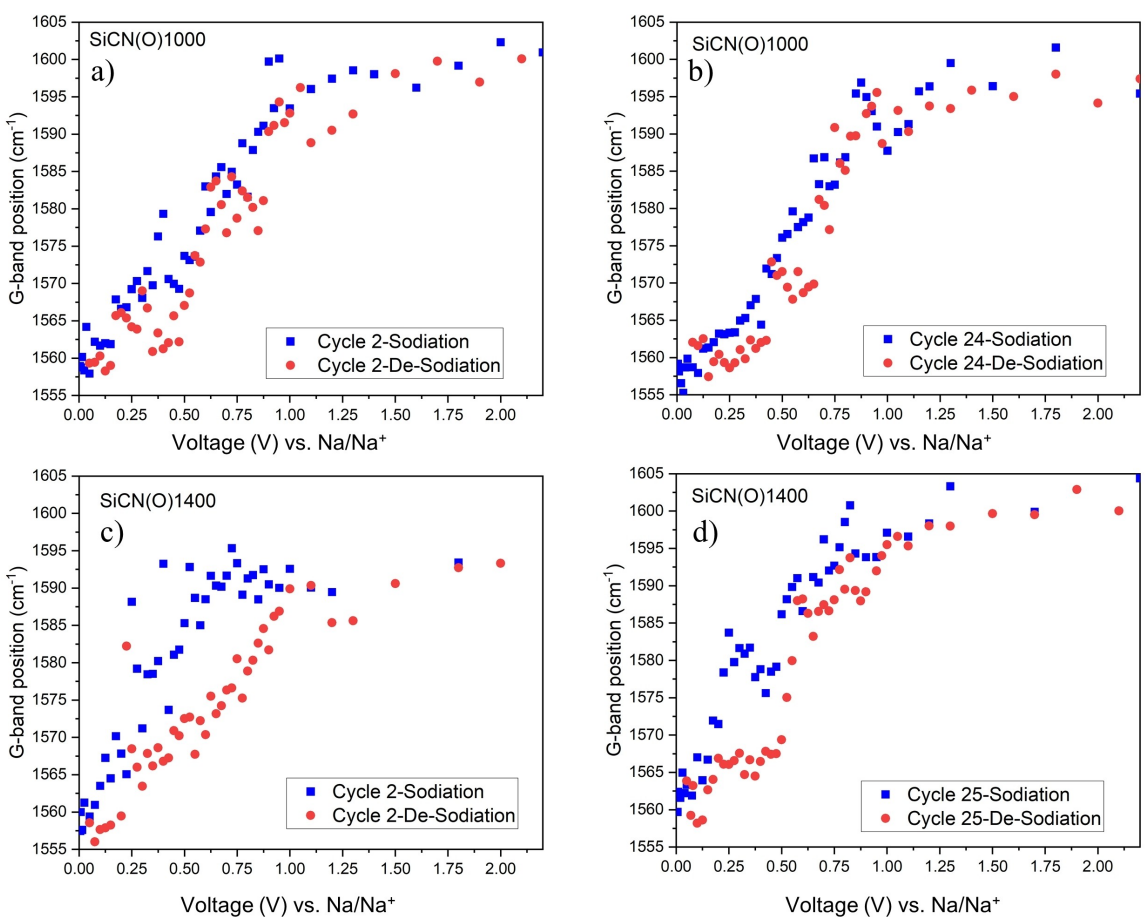


Figure 7. G-band position shift along sodiation and de-sodiation during the initial cycle a,c) and after more than 20 cycles b,d) for both samples.

mechanism is underlined by lower efficiencies of the sodiation/de-sodiation process in SiCN(O)1400 as visible in Table 6.

Along cycling, multiple factors including residual Na doping of the “free carbon”, growing internal tension and a change of the disposition and structure of the disordered carbon may contribute to permanent band shifts by influencing the vibrations of the atoms in the carbon and therefore the resulting energy of the emitted photon.^[48–51] These findings demonstrate that SiCN(O)1000 can effectively accommodate and release sodium ions without causing permanent modifications to its structure. However, the higher surface area due to higher porosity of SiCN(O)1400 obviously contributes to increased sodium ion trapping within its pores potentially impacting the reversibility of the sodiation and de-sodiation processes.

Conclusions

This study explored the impact of the microstructural modifications originated from a different thermal treatment on the sodium intercalation in a SiCN(O) ceramic matrix. Two samples produced using different thermal treatments, namely i) pyrolysis at 1000 °C and ii) pyrolysis at 1000 °C + annealing at 1400 °C were characterized. The crystallite size of the disordered carbon embedded in the pristine materials (5.1 nm for SiCN(O)1000 and 6.8 nm for SiCN(O)1400) were compared with a fructose-derived hard carbon (6.3 nm) evidencing structural similarity. Chemical composition analysis revealed that the carbothermal reduction at 1400 °C leads to the formation of electrochemically inactive crystalline β-SiC at the cost of amorphous mixed-bond structures (SiC_xN_yO_z). This results in a reduced capacity of the sample SiCN(O)1400 (52.3 mAh/g) compared to SiCN(O)1000 (112.4 mAh/g). An additional consequence of the carbothermal reduction is the increased porosity and internal surface area of the SiCN(O)1400 (331 m²/g) sample compared to that of SiCN(O)1000 (56.7 m²/g). The sodium insertion process in the “free carbon” embedded in the silicon oxycarbonitride (SiCN(O)) matrix and its dependence on the material microstructure have been investigated with operando Raman spectroscopy. The results demonstrate a storage process in the embedded carbon that aligns with previous findings on Na storage in HCs, relying

Table 6. Efficiencies of sodiation/de-sodiation processes during the in-situ measurements.

Sample	Efficiency (%)		
	Cycle 1 (SEI)	Cycle 2	Cycle 24/25
SiCN(O)1000	24.8	75.8	96.4
SiCN(O)1400	17.4	57.6	93.7

on the insertion of ions into its disordered structure. The comparison of the band shift positions along cycling between the two ceramics evidences a reduced reversibility of the insertion process for the SiCN(O)1400 which we attribute to the higher internal surface, enhanced porosity and reduced size of the pores. These microstructural modifications induce the irreversible trapping of Na-ions in the matrix decreasing therefore the capacity and efficiency of the process. Our findings contribute to a deeper understanding of the sodium insertion mechanism in SiCN(O) and provide valuable insights into the role of "free carbon" and its microstructure in the storage mechanism.

Acknowledgements

The authors gratefully acknowledge the financial support by the EU-Project SIMBA (Sodium-Ion and Sodium-Metal Batteries for efficient and sustainable next-generation energy storage (<https://simba-h2020.eu>), Grant Number: 963542. Alexander Kempf and Magdalena Graczyk-Zajac gratefully acknowledge the financial support by the German Research Foundation (DFG) in the frame of the BEETHOVEN Classic 3 – Polish-German Funding Initiative (GR 4440/4-1). Open Access funding enabled and organized by Projekt DEAL.

Conflict of Interests

The authors have no conflict of interest to declare.

Data Availability Statement

The data that support the findings of this study are available from the corresponding author upon reasonable request.

Keywords: Sodium • Polymer-derived Ceramics • Storage Mechanism • Raman Spectroscopy • Embedded Amorphous Carbon

- [1] L. Bongartz, S. Shammugam, E. Gervais, T. Schlegl, *J. Cleaner Prod.* **2021**, 292, 126056, doi: 10.1016/j.jclepro.2021.126056.
- [2] CB. Tabelin, J. Dallas, S. Casanova, T. Pelech, G. Bournival, S. Saydam, I. Canbulat, *Miner. Eng.* **2021**, 163, 106743, doi: 10.1016/j.mineng.2020.106743.
- [3] J. Peters, A. Peña Cruz, M. Weil, *Batteries* **2019**, 5, 10, doi: 10.3390/batteries5010010.
- [4] M. R. B. Domalanta, M. T. Castro, J. A. D. Del Rosario, J. D. Ocon, *Chemical Engineering Transactions* **2022**, 94, 139-44, doi: 10.3303/CET2294023.
- [5] P. Colombo, *Science* **2008**, 322, 381–3, doi: 10.1126/science.1162962.
- [6] R. Kolb, C. Fasel, V. Liebau-Kunzmann, R. Riedel, *J. Eur. Ceram. Soc.* **2006**, 26, 3903–8, doi: 10.1016/j.jeurceramsoc.2006.01.009.
- [7] LM. Reinold, M. Graczyk-Zajac, Y. Gao, G. Mera, R. J. Riedel, *Power Sources* **2013**, 236, 224–9, doi: 10.1016/j.jpowsour.2013.02.046.
- [8] M. Graczyk-Zajac, G. Mera, J. Kaspar, R. Riedel, *J. Eur. Ceram. Soc.* **2010**, 30, 3235–43, doi: 10.1016/j.jeurceramsoc.2010.07.010.
- [9] S.-H. Baek, L. M. Reinold, M. Graczyk-Zajac, R. Riedel, F. Hammerath, B. Büchner, H.-J. Grafe, *J. Power Sources* **2014**, 253, 342–8, doi: 10.1016/j.jpowsour.2013.12.065.
- [10] J. Kaspar, G. Mera, A. P. Nowak, M. Graczyk-Zajac, R. Riedel, *Electrochim. Acta* **2010**, 56, 174–82, doi: 10.1016/j.electacta.2010.08.103.
- [11] F. Qu, M. Graczyk-Zajac, D. Vrankovic, N. Chai, Z. Yu, R. Riedel, *Electrochim. Acta* **2021**, 384, 138265, doi: 10.1016/j.electacta.2021.138265.
- [12] L. M. Reinold, Y. Yamada, M. Graczyk-Zajac, H. Munakata, K. Kanamura, R. Riedel, *J. Power Sources* **2015**, 282, 409–15, doi: 10.1016/j.jpowsour.2015.02.074.
- [13] J. Kaspar, M. Storch, C. Schitco, R. Riedel, M. Graczyk-Zajac, *J. Electrochem. Soc.* **2016**, 163, A156–A162, doi: 10.1149/2.0391602jes.
- [14] M. Melzi d'Eril, A. Zambotti, M. Graczyk-Zajac, E. Ionescu, G. D. Soraru, R. Riedel, *Open Ceramics* **2023**, 14, 100354, doi: 10.1016/j.oceram.2023.100354.
- [15] A. Kempf, S. Kiefer, M. Graczyk-Zajac, E. Ionescu, R. Riedel, *Open Ceramics* **2023**, 15, 100388, doi: 10.1016/j.oceram.2023.100388.
- [16] D. M. Soares, G. Singh, *Nanotechnology* **2020**, 31, 145403, doi: 10.1088/1361-6528/ab6480.
- [17] R. Sujith, J. Gangadhar, M. Greenough, R. K. Bordia, D. K. Panda, *J. Mater. Chem. A* **2023**, 11, 20324–48, doi: 10.1039/D3TA01366A.
- [18] M. Melzi d'Eril, M. J. Graczyk-Zajac, R. Riedel, *Batteries & Supercaps* **2023**, 6, 3, doi: 10.1002/batt.202200491.
- [19] J. Kaspar, M. Graczyk-Zajac, S. Choudhury, R. Riedel, *Electrochim. Acta* **2016**, 216, 196–202, doi: 10.1016/j.electacta.2016.08.121.
- [20] C. Chandra, J. Kim, *Chem. Eng. J.* **2018**, 338, 126–36, doi: 10.1016/j.cej.2018.01.032.
- [21] X. Cheng, H. Li, Z. Zhao, Y. Wang, X. Wang, *New. Carbon. Mater.* **2021**, 36, 93–105, doi: 10.1016/S1872-5805(21)60007-0.
- [22] P. J. Nohrinen, C. Korte, *Anal. Chem.* **2019**, 91, 8054–61, doi: 10.1021/acs.analchem.8b05819.
- [23] J. R. Rodriguez, S. B. Aguirre, V. G. Pol, *Electrochim. Acta* **2019**, 319, 791–800, doi: 10.1016/j.electacta.2019.07.030.
- [24] T. E. Rosser, E. J. F. Dickinson, R. Raccichini, K. Hunter, A. D. Searle, C. M. Kavanagh, et al., *J. Electrochem. Soc.* **2021**, 168, 70541, doi: 10.1149/1945-7111/ac132d.
- [25] G. Mera, A. Navrotsky, S. Sen, H.-J. Kleebe, R. Riedel, *J. Mater. Chem. A* **2013**, 1, 3826, doi: 10.1039/c2ta00727d.
- [26] D. Vrankovic, M. Storch, C. Schitco, Z. M. Graczyk, R. Riedel, Verfahren zum Herstellen poröser Keramiken und eines porösen Keramikprodukts; 9/7/2016.
- [27] M. Graczyk-Zajac, L. M. Reinold, J. Kaspar, P. V. W. Sasikumar, G.-D. Soraru, R. Riedel, *Nanomaterials* **2015**, 5, 233–45, doi: 10.3390/nano5010233.
- [28] G. D. Soraru, S. Modena, E. Guadagnino, P. Colombo, J. Egan, C. Pantano, *Journal of the American Ceramic Society* **2002**, 85, 1529–36, doi: 10.1111/j.1151-2916.2002.tb00308.x.
- [29] L. G. Cançado, K. Takai, T. Enoki, M. Endo, Y. A. Kim, H. Mizusaki, et al., *Appl. Phys. Lett.* **2006**, 88, 163106, doi: 10.1063/1.2196057.
- [30] K. Pfeifer, S. Arnold, Ö. Budak, X. Luo, V. Presser, H. Ehrenberg, S. Dsoke, *J. Mater. Chem. A* **2020**, 8, 6092–104, doi: 10.1039/d0ta00254b.
- [31] R. E. Ruther, K. A. Hays, S. J. An, J. Li, D. L. Wood, J. Nanda, *ACS Appl. Mater. Interfaces* **2018**, 10, 18641–9, doi: 10.1021/acsami.8b02197.
- [32] J. S. Weaving, A. Lim, J. Millichamp, T. P. Neville, D. Ledwoch, E. Kendrick, et al., *ACS Appl. Energ. Mater.* **2020**, 3, 7474–84, doi: 10.1021/acsam.0c00867.
- [33] L. G. Cançado, A. Jorio, E. H. M. Ferreira, F. Stavale, C. A. Achete, R. B. Capaz, et al., *Nano Lett.* **2011**, 11, 3190–6, doi: 10.1021/nl201432g.
- [34] R. Nandan, N. Nakamori, K. Higashimine, R. Badam, N. Matsumi, *J. Mater. Chem. A* **2022**, 10, 5230–43, doi: 10.1039/DITA08516F.
- [35] Z. Chen, M. Zhou, Y. Cao, X. Ai, H. Yang, J. Liu, *Adv. Energy Mater.* **2012**, 2, 95–102, doi: 10.1002/aenm.201100464.
- [36] Y. Yang, J.-G. Ren, X. Wang, Y.-S. Chui, Q.-H. Wu, X. Chen, W. Zhang, *Nanoscale* **2013**, 5, 8689–94, doi: 10.1039/C3NR02788K.
- [37] J. Kaspar, M. Graczyk-Zajac, R. J. Riedel, *Power Sources* **2013**, 244, 450–5, doi: 10.1016/j.jpowsour.2012.11.086.
- [38] D. B. Schuepfer, F. Badaczewski, J. M. Guerra-Castro, D. M. Hofmann, C. Heiliger, B. Smarsly, P. J. Klar, *Carbon* **2020**, 161, 359–72, doi: 10.1016/j.carbon.2019.12.094.
- [39] M. A. Reddy, M. Helen, A. Groß, M. Fichtner, H. Euchner, *ACS Energy Lett.* **2018**, 3, 2851–7, doi: 10.1021/acsenergylett.8b01761.
- [40] F. Joucken, L. Henrard, J. Lagoute, *Phys. Rev. Materials* **2019**, 3, 11, doi: 10.1103/PhysRevMaterials.3.110301.
- [41] F. Tuinstra, J. L. Koenig, *J. Chem. Phys.* **1970**, 53, 1126–30, doi: 10.1063/1.1674108.
- [42] C. Thomsen, S. Reich, *Phys. Rev. Lett.* **2000**, 85, 5214–7, doi: 10.1103/PhysRevLett.85.5214.

- [43] R. N. Gontijo, G. C. Resende, C. Fantini, B. R. Carvalho, *J. Mater. Res.* **2019**, *34*, 1976–92, doi: 10.1557/jmr.2019.167.
- [44] P. Venezuela, M. Lazzari, F. Mauri, *Phys. Rev. B* **2011**, *84*, 3, doi: 10.1103/PhysRevB.84.035433.
- [45] R. Saito, M. Hofmann, G. Dresselhaus, A. Jorio, M. S. Dresselhaus, *Adv. Phys.* **2011**, *60*, 413–550, doi: 10.1080/00018732.2011.582251.
- [46] C. A. Howard, M. P. M. Dean, F. Withers, *Phys. Rev. B* **2011**, *84*, 24, doi: 10.1103/PhysRevB.84.241404.
- [47] M. S. Dresselhaus, G. Dresselhaus, *Advances in Physics* **2002**, *51*, 1–186, doi: 10.1080/00018730110113644.
- [48] D. Tuschel, *Spectroscopy* **2017**, *32*, 13–8.
- [49] M. W. Iqbal, M. Z. Iqbal, M. F. Khan, X. Jin, C. Hwang, J. Eom, *Sci. Technol. Adv. Mater.* **2014**, *15*, 55002, doi: 10.1088/1468-6996/15/5/055002.
- [50] P. M. Mummary, R. Krishna, *Spectroscopy* **2018**, *33*, 30–3.
- [51] A. Das, S. Pisana, B. Chakraborty, S. Piscanec, S. K. Saha, U. V. Waghmare, et al., *Nat. Nanotechnol.* **2008**, *3*, 210–5, doi: 10.1038/nnano.2008.67.

Manuscript received: January 17, 2024
Revised manuscript received: March 5, 2024
Version of record online: March 27, 2024
